Geophysical Research Letters

RESEARCH LETTER
10.1029/2018GL081766

Key Points:
- The focal mechanisms of induced earthquake swarms near Fox Creek support a flower type of fault structure striking N-S orientation
- Both faults and hydraulic fractures can affect regional crustal seismic anisotropy
- Loss of fluid into the fault damage zone is responsible for the observed spatiotemporal variation of seismic anisotropy

Supporting Information:
- Supporting Information S1

Correspondence to:
Y. J. Gu and Z. Wang,
ygu@ualberta.ca;
wangzzh@upc.edu.cn

Citation:
Li, T., Gu, Y. J., Wang, Z., Wang, R., Chen, Y., Song, T.-R. A., & Wang, R. (2019). Spatiotemporal variations in crustal seismic anisotropy surrounding induced earthquakes near Fox Creek, Alberta. *Geophysical Research Letters*, *46*. https://doi.org/10.1029/2018GL081766

Received 13 JAN 2019
Accepted 24 APR 2019
Accepted article online 30 APR 2019

©2019. American Geophysical Union. All Rights Reserved.

Spatiotemporal Variations in Crustal Seismic Anisotropy Surrounding Induced Earthquakes Near Fox Creek, Alberta

Tianyang Li[1,2,3], Yu Jeffrey Gu[2], Zizhen Wang[1,3], Ruijia Wang[2,4], Yunfeng Chen[2], Teh-Ru Alex Song[5], and Ruihe Wang[1,3]

[1]Key Laboratory of Unconventional Oil & Gas Development (China University of Petroleum [East China]), Ministry of Education, Qingdao, China, [2]Department of Physics, University of Alberta, Edmonton, Alberta, Canada, [3]School of Petroleum Engineering, China University of Petroleum (East China), Qingdao, China, [4]Department of Earth Sciences, Western University, London, Ontario, Canada, [5]Department of Earth Sciences, University College London, London, UK

Abstract This study analyzes earthquake recordings from four near-source (<10 km) stations near Fox Creek, Alberta, a region known for hydraulic fracturing-induced seismicity. We examine the spatiotemporal variations of focal mechanisms and seismic anisotropy in the sedimentary strata. The focal mechanisms of surrounding earthquake swarms are generally consistent with the strike-slip mechanism of the M_L 4.6 earthquake, favoring a flower type of fault structure. The NE-SW-orientated fast splitting direction, determined from the shear wave splitting measurements, reflects the combined effects of (1) N-S faults and (2) NE-SW time-dependent hydraulically stimulated fractures. The latter effect dominates the apparent anisotropy during the days leading to the mainshock, while its contributions are reduced by 60–70% after the mainshock. Loss of fluid into the fault damage zone, which causes the closure of fractures, is responsible for the observed spatiotemporal variation of seismic anisotropy near the hydraulic fracturing well.

Plain Language Summary The classic method that measures the travel time and polarization differences between two polarized shear waves, known as "shear wave splitting," is widely used to determine directional-dependent seismic wave speeds (i.e., anisotropy) at both global and exploration scales. This study takes advantage of industry data to measure and characterize the seismic anisotropy surrounding a hydraulic fracturing well near Fox Creek, Alberta. We analyze the induced seismicity and examine the earthquake source types and anisotropy in the sedimentary strata. The source mechanism confirms the previously reported N-S striking, flower-type fault system. The decreasing seismic anisotropy over time is most likely caused by the closures of hydraulic fractures surrounding the hydraulic fracturing well. This result is critical to the understanding of local seismic anisotropy, for both regulatory agencies and the industry.

1. Introduction

The Alberta basin has experienced increased levels of induced earthquakes associated with hydraulic fracturing (HF) stimulation in recent years (Atkinson et al., 2016; Schultz et al., 2018), most notably within the Duvernay Formation (the largest shale gas formation in central Alberta) near the town of Fox Creek, Alberta (Bao & Eaton, 2016; Schultz et al., 2017). One likely triggering mechanism is fluid migration along the fault damage zone (Galloway et al., 2018) via existing hydrological connections between the HF networks and macroscopic faults (Ellsworth, 2013; Grigoli et al., 2018; Langenbruch & Zoback, 2016). The strike-slip focal mechanisms of the HF-induced earthquakes (Figure 1) in central-southern Alberta have direct implications for the sizes and orientations of reactivated fault zones, and seismic moment tensors of regional earthquakes show approximately NE-oriented P axes (Schultz et al., 2017; Wang et al., 2016, 2018).

The presence of aligned fractures or faults can result in seismic anisotropy (Faccenda et al., 2008; Savage, 1999; Silver & Chan, 1991), which has been widely used to infer the subsurface stress field and crustal geology (Kaneshima, 1990; Licciardi et al., 2018). One of the classic methods to detect seismic anisotropy is shear wave splitting, which measures the travel time and polarization differences between fast and slow *S* waves in an anisotropic medium. Previous studies conducted in Alberta consistently reported the existence of azimuthal anisotropy in western Canada at lithospheric depths: The upper-mantle anisotropy is

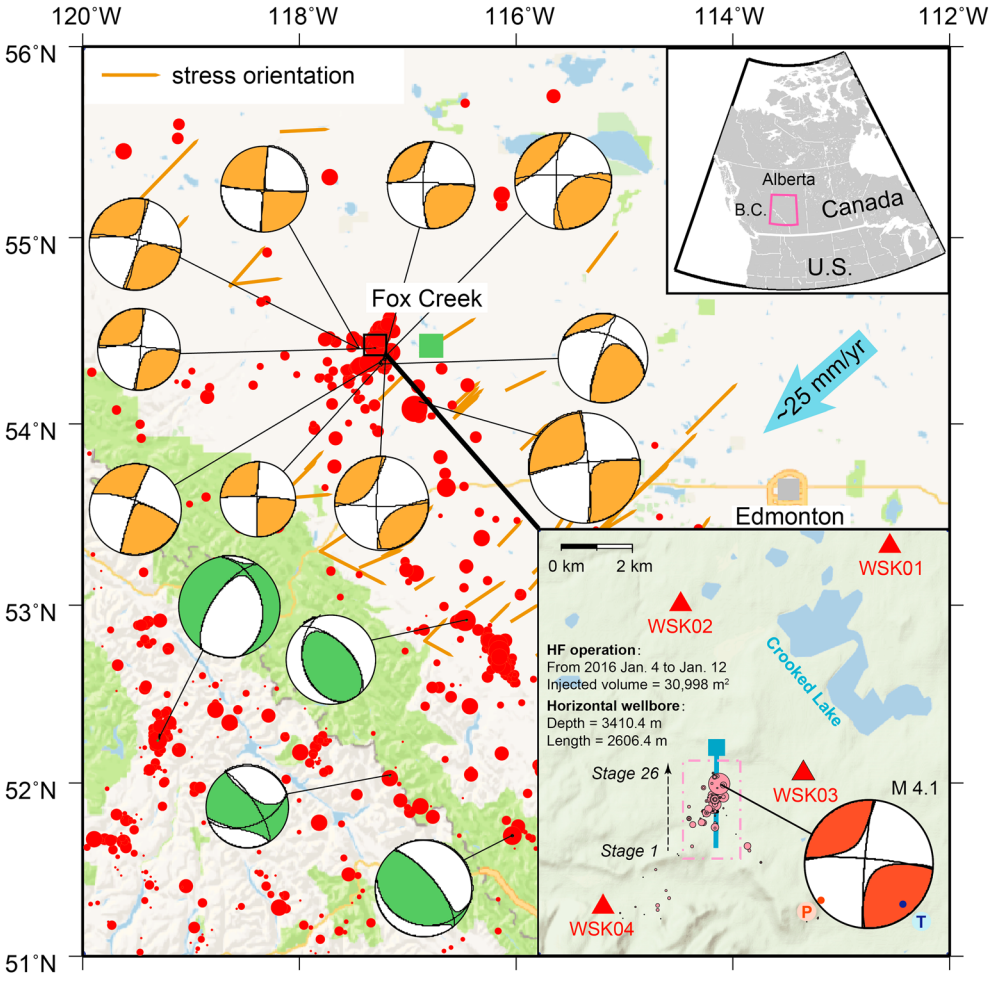

Figure 1. Distribution of the stations (triangles) and earthquakes (red circles) in the study region near Fox Creek, Alberta. The blue arrow indicates the current direction and rate of plate motion. The focal mechanisms are grouped into tectonic (green) and HF-induced (orange) earthquakes. Crustal stress orientations obtained from borehole breakouts (Barth et al., 2010) are indicated by the brown-colored lines. The pink circles within the dotted rectangle indicate the induced earthquakes in January 2016.

mostly aligned along an NE-SW orientation according to SKS splitting measurements from teleseismic arrivals, which is roughly parallel to the direction of absolute plate motion (Courtier et al., 2010; Saruwatari et al., 2001; Shragge et al., 2002; Wu et al., 2019). Crustal anisotropy, on the other hand, is usually stress- (Crampin, 1991; Gavin & Lumley, 2016) or structure-induced (Licciardi et al., 2018; Meadows & Winterstein, 1994), especially in the upper crust (Balfour et al., 2012; Tarayoun et al., 2017). At local scales, anisotropy can result from the preferential opening of microscale, fluid-filled fractures under the maximum horizontal compressive stress (Crampin, 1987; Kaneshima et al., 1988) and deformation-induced, crystal-preferred orientation along preexisting faults or folds (Eken et al., 2013; Licciardi et al., 2018). Typically, rock formations of the crust are assumed to be transversely isotropic for long-wavelength seismic waves in anisotropy analyses. Whether this simple form of crustal seismic anisotropy applies to the Duvernay play remains unsolved due to the relatively sparse broadband station coverage and limited public access to 3-D seismic data. Temporal and spatial variations of seismic anisotropy have been reported near the epicenter of a natural earthquake (Kaviris et al., 2017; Peng & Ben-Zion, 2005). Our focus is the region surrounding a seismogenic HF well (Figure 1) near Fox Creek, Alberta, based on (1) the focal mechanisms and (2) shear wave splitting measurements using continuous waveforms from an M_L 4.6 (Mw 4.1, January 2016) earthquake sequence recorded by four near-source (<10 km) stations.

2. Data and Methods

Triggered by HF stimulations, hundreds of earthquakes have been detected on the reactivated faults near Fox Creek since 2013 (Bao & Eaton, 2016). For the M_L 4.6 mainshock (the largest magnitude event in the sequence) on 12 January 2016, over 400 events within 3 weeks were identified by Wang et al. (2017) surrounding the suspected HF well (Figure 1). This event was also known as the second "red-light" earthquake ("traffic-light" protocol; Subsurface Order 2, Alberta Energy Regulator). To assess the robustness and time-sensitive variations in earthquake faulting parameters, we focus on the detected events from 4 to 19 January 2016 and use S-P differential travel times to verify the relative event-station locations (and distances). Subsequently, we combine the nearby events in the magnitude range of $0.6 < M_L < 2.0$ into clusters and select two stimulated clusters (HF1 and HF2) during the HF stimulation and two poststimulation clusters (POST1 and POST2) (see Text S1.1 in the supporting information). The distances of these four clusters are less than 0.9 km to the mainshock and 0.4 km to the nearby HF well. The number of collocated events in each cluster ranges from 7 to 10, and all events within each cluster share a high degree of waveform similarity (correlation coefficient > 0.8). The HF1 and HF2 clusters occurred during the HF stimulation and prior to the mainshock, whereas the clusters POST1 and POST2 were detected after the last stage of the HF (see Figure S3 for the time span of the clusters).

Recent studies show that most of the induced seismicity in central Alberta is dominated by strike-slip/thrust faulting mechanisms, whereas limited nondouble-couple components are related to fluid injection (Eaton et al., 2018; Wang et al., 2018). To assess the spatiotemporal changes in faulting characteristics in our study, the focal mechanism solutions were determined by fault-related (double-couple) mechanisms using P-, SH-, and SV-wave first-motion polarities and amplitude information (Snoke, 1984) from waveforms recorded at four stations. The amplitudes are measured from the first motions on the stacked displacement seismograms in each cluster, and the polarities are determined from the rotated (vertical, radial, and transverse) three-component seismograms (see Text S1.2). For each event, we obtain at least 10 polarities and 5 amplitude ratios, and the wide azimuthal distribution of the four stations provides robust first-order constraints on the focal mechanisms.

We characterize anisotropy by shear wave splitting parameters that consist of the polarization of the fast *S* wave Φ and the splitting time δt between the fast and slow *S* waves following the rotation correlation method (Bowman & Ando, 1987; Long & Silver, 2009; see Text S1.3). This approach searches for the optimal parameter Φ to maximize the waveform similarity between the two *S* waves and measures δt between them. The step width of the grid search is 1.0° for Φ and 0.01 s for δt. The δt can be scaled to the path length to provide an estimate of the average anisotropy along the ray path (Silver & Chan, 1988). All of the seismograms are band-pass filtered with corner frequencies of 2–6 Hz to emphasize the local *S* waves (Huang et al., 2011; Saltzer et al., 2000). We only consider station-event pairs with incidence angles <30° from the vertical to eliminate spurious results with particle motions contaminated by surface-converted phases (Booth & Crampin, 1985). Consequently, we reject shear wave splitting measurements at the relatively distant station (~10 km) WSK01 with an average incidence angle of 32°. The final data set contains 32 events, resulting in 96 high-quality source-station pairs for the splitting analysis.

3. Focal Mechanism Solutions and Shear Wave Splitting Observations

3.1. Overall Results

The average focal mechanism of each event cluster is obtained from the polarities and amplitudes of high-frequency body waves recorded by the four stations (Figure 2a). To determine these parameters, all waveforms are first stacked for each cluster (Figure 2b). The fault plane solution of the M_L 4.6 mainshock shows a right-lateral strike-slip mechanism, consistent with that of the mainshock from an earlier regional moment tensor inversion using low-frequency waveforms (Schultz et al., 2017). The clusters HF1, HF2, and POST1 share similar strike-slip focal mechanisms (strike = 196° ± 3°, rake = 165° ± 5°) with dipping angles >84°, whereas cluster POST2 exhibits a dominant oblique strike-slip (strike = 204° ± 5°, rake = −153° ± 5°) mechanism with minor normal-faulting components (i.e., dipping angle of 51° ± 5°).

Most importantly, the faulting parameters (e.g., geometry and slip) of the four clusters do not exhibit apparent temporal variations. This implies that temporal changes in splitting measurements are mainly

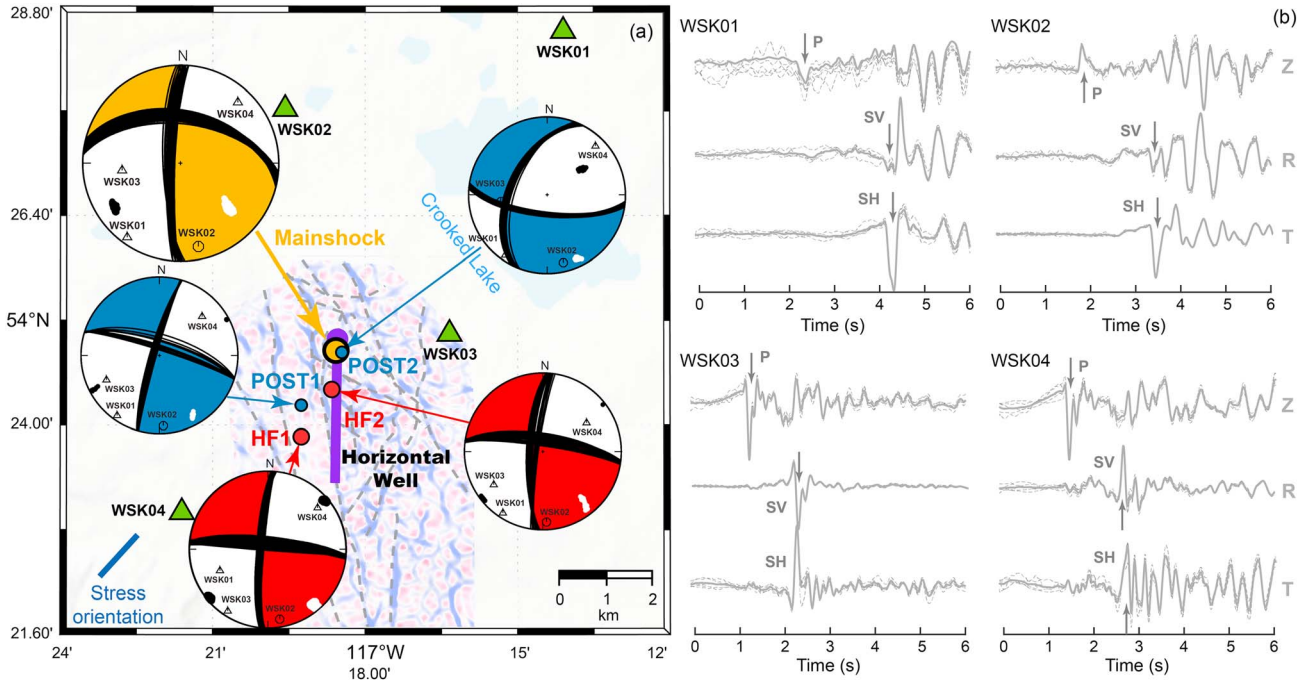

Figure 2. (a) Focal mechanism solutions of four clusters of earthquakes in January 2016. All possible focal nodal planes are indicated by the black lines, and the P polarities (triangles, hexagons) and P and T axes (black and white dots, respectively) are as labeled. The horizontal slice of the reported curvature volume (see Figure 17 in Chopra et al., 2017) provides the apparent distribution of faults at the basement level. (b) The stacked vertical-, radial-, and transverse-component recordings at each station for cluster HF1. The arrows indicate the polarities of P-, SV-, and SH-waves.

influenced by the structural variations along the ray paths rather than the earthquake radiation patterns. We subsequently determine the optimal pairs of Φ and δt for the representative splitting measurements based on robust S waveforms from the input seismograms (Figure 3a). The fast and slow S waves are well-aligned after correcting the splitting effect, and their particle motion becomes linear (Figure 3b). These observations and the energy map of T component with limited error (Figure 3c) are evidence of a well-constrained splitting measurement (Teanby et al., 2004). Figure 3d shows the average values with low error bounds (less than 18° and 0.015 s at the 95% confidence level) for the apparent fast splitting directions and splitting times for stations WSK02, WSK03, and WSK04.The δt varies from 0.01 to 0.07 s, which is comparable to those expected from a typical anisotropic crust (i.e., δt ~ 0.1 s; Savage, 1999) at the depth range of 0–3.5 km. Except at station WSK04, the NE-SW fast splitting directions remain nearly unchanged after the mainshock. Most notably, the splitting time measured from the near-well cluster HF2 is on the order of 0.06 s. After the mainshock, there is a 60–70% reduction in δt (to 0.02 s) and deviates of ~25° in the fast splitting directions (to 10–12°) at this station. The average anisotropy ($\frac{\delta t}{\sum_{i=1}^{n} \frac{d_i}{V_{Si}}}$, where d_i is the ray path length within each layer and V_{Si} is the corresponding S wave velocity) for cluster HF2 is 2–2.5%, which is larger than the average anisotropy of 0.6–0.7% for cluster HF1 (see Figure 3d). At station WSK03, we obtain null measurements from clusters HF1 and HF2 at the back azimuth of ~250°. This suggests that the symmetry axis is likely parallel or normal to the back azimuth between station WSK03 and the two clusters (Long & Silver, 2009).

3.2. Sensitivity Analysis

We compare the splitting-corrected S wave polarization against the S wave initial polarization predicted from the focal mechanism (e.g., Ando et al., 1983) and examine the robustness of splitting measurements. Synthetic seismograms are calculated with well-resolved focal mechanisms, which are constrained by high-quality waveforms from a wide azimuthal coverage (see Text S2) and a refined regional velocity model (Wang et al., 2017). The particle motion of synthetic S waves (the green line in Figures S9–S20) is linear,

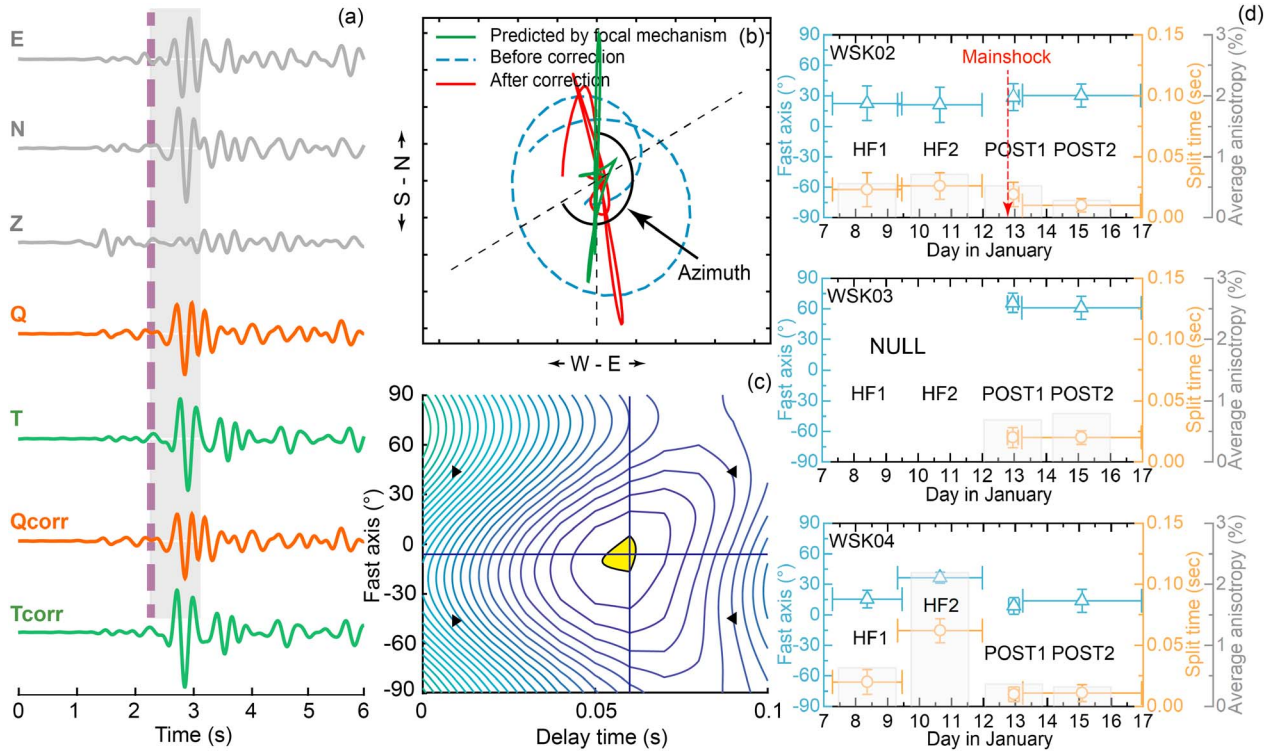

Figure 3. Shear wave splitting measurements. (a) The recorded seismograms of one event in HF2 cluster at WSK04 in the NEZ coordinate system (grey lines) and the corresponding Q and T seismograms (colored lines). The corrected waveforms (after removing the split time differences between fast and slow polarizations) are labeled as Qcorr and Tcorr. The optional time window of the shear wave splitting analysis is marked by the purple-colored line and shaded area. (b) Particle motion of the fast and slow *S* waves before (dotted blue line) and after (solid red line) the correction. The green line shows the *S* wave polarization predicted from the synthetic waveforms. (c) Contour map of the energy of the corrected T component where the optimal splitting parameters are associated with the minimum energy. The 95% confidence interval is indicated by the cross area of yellow shading. (d) The splitting and null measurements at the three stations. The vertical error bars denote standard deviations associated with the average results, and the horizontal error bars show the period of the four clusters.

consistent with the prediction from an isotropic input velocity model. The general consistency between the predicted *S* wave polarization and the splitting-corrected *S* wave polarization (the red line in Figures S9–S20) verifies the robustness of the focal mechanism solution and splitting measurements. As an example, the predicted initial *S* wave polarization from the synthetic seismogram at station WSK04 (the green line in Figure 3b) agrees with the splitting-corrected *S* wave polarization from the observation (N-S direction, the red line in Figure 3b) to within 10°. Their difference is potentially caused by (1) nondouble-couple components (usually <20%) that are not included in the focal mechanism to generate the synthetic waveforms, (2) the lack of a detailed sedimentary velocity model that affects the accuracy of the phase arrivals, and (3) the influence of anisotropy on the radiation pattern of *S* wave and the focal mechanism solution (Ben-Menahem et al., 2007; Rößler et al., 2007). Nevertheless, the lack of detectable time delay (<0.01 s) in these synthetic waveforms also indicates that the bulk of the observed split time (~0.06 s) is associated with seismic anisotropy in the shallow crust.

4. Discussion

4.1. Stimulated Seismicity

A detailed examination of the solutions reveals two dominant focal mechanisms within the four clusters. The clusters located west of the mainshock (i.e., HF1, HF2, and POST1) share a nearly pure N-S strike-slip focal mechanism, whereas the eastern cluster (POST2) exhibits an apparent oblique slip on a nonvertical fault plane. The spatial variation of focal mechanisms among different clusters is consistent with a flower type of fault structure proposed by previous studies (Chopra et al., 2017; Eaton et al., 2018; Wang et al., 2017; Zhang et al., 2019). The P axes of our resolved focal mechanisms are aligned along the NE-SW

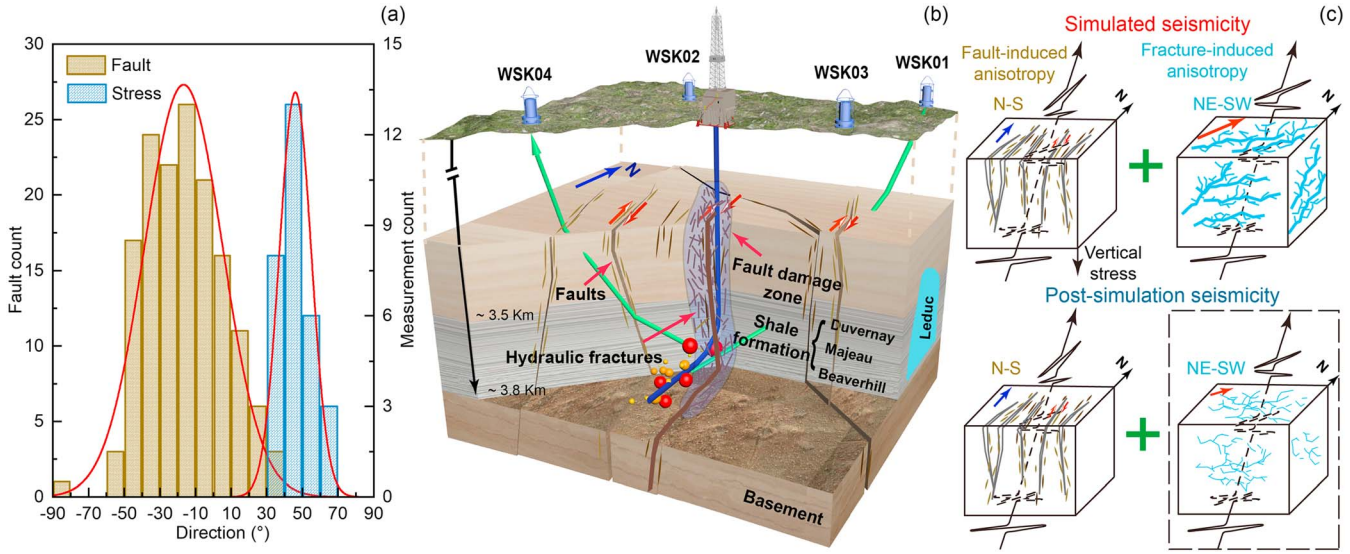

Figure 4. Interpretation of the two types of anisotropy. (a) Distribution of maximum crustal compressive stress directions based on borehole breakouts (Murray & Schmitt, 2016) and focal mechanisms of regional earthquakes (Wang et al., 2017). The histogram of fault direction is extracted from the slice in Figure 2 with the Standard Hough Transform (Ballard, 1981; Figure S21). The red lines show the best-fit Gaussian distributions of the histograms. (b) A 3-D structural model with faults and fractures in our study area. The major buried faults in this region are oriented roughly in an N-S orientation, whereas the fluid-filled fractures surrounding the horizontal well exhibit NE-SW directions that are parallel to that of the maximum horizontal stress. The ray paths (green lines) are influenced by the source-station distance. (c) Anisotropy induced by the faults (brown lines) and fluid-filled fractures (blue lines) before (upper) and after (lower) the mainshock. The contributions of fracture-induced anisotropy are reduced (dotted rectangle) after the mainshock due to fluid loss.

direction, also consistent with the orientation of regional maximum horizontal stress (with a median of 51°, Figure 4a).

It has been suggested that shear wave splitting is often controlled by nonuniform anisotropic properties in regional crustal settings (Park & Levin, 2002; Saltzer et al., 2000). In our case, there are two possible causes for shear wave splitting. First, crystal-preferred orientations resulting from deformation along preexisting regional geological structures, such as the small-scale faults or folds (Li & Peng, 2017; Maher & Kendall, 2018), can influence the wavespeed (timing) of shear waves against polarization directions (Silver, 1996). The approximately N-S-aligned normal faults exhibit Gaussian distributions with wide strike orientations ranging from N50°W to N40°E (Figure 4a). Second, stress-aligned fluid-filled fractures in the shale formation (which are often associated with HF stimulation) can produce a fast splitting direction parallel to fracture orientation (Anderson et al., 1974; Li et al., 2016; Nolte et al., 2017). These two types of anisotropy may be distinguishable from their depths: The latter scenario with fractures aligned approximately with the NE-SW maximum horizontal stress (Figure 4a) may result in anisotropy in the vicinity of the HF (typically 3- to 4-km depth for Duvernay around Fox Creek), whereas fault-induced anisotropy could potentially extend from the basement (considering the fault is deep-seated) to the subsurface and affect the entire ray path. Based on the relationships between the magnitude and rupture area (Wells & Coppersmith, 1994), a 1-km fault is sufficient to produce M_L 4.6 mainshock (Wang et al., 2018), and small-scale faults with dimensions of dozens of meters are capable of producing the M_L = 0.6–2 events. Similarly, field microseismic fracture mapping has suggested that the half-length of hydraulic fractures can reach up to 150 m in shale layers (Fischer et al., 2008; Nagel et al., 2013), comparable to the wavelengths of 2- to 6-Hz seismic waves in our analyses. As measurements from HF1 correspond mostly at the earlier stage of the HF than those from HF2, they likely have experienced greater effects from the fluid-filled fractures. Taking their overlapped path geometries into consideration, the differences in anisotropy (by ~0.04 s) in this study mainly result from the region around the source area (i.e., area between HF1 and HF2).

For far-field station WSK02, the δt from HF2 is slightly larger than that from HF1 (see Figure 3d) despite a shorter distance between HF2 and the station. Furthermore, the differences (<0.01 s) between HF1 and HF2 from WSK02 are much smaller than those from WSK04, which are The spatial variationpartly caused by the difference in the acute angle between the anisotropic symmetry axis and source-station ray paths (i.e.,

approximately normal and parallel to the direction of fluid-filled fractures for WSK02 and WSK04, respectively). Observations of small δt toward the NW (WSK02) and large δt toward the SW (WSK04) are not necessarily unexpected for an inclined fractured layer with an NW-tilted slow symmetry axis (Ando et al., 1983; Song & Kawakatsu, 2012). Since the immediate vicinity of HF represents only a small fraction of the total *S* wave ray paths, its temporal changes in the strength of anisotropy is much greater than that distributed along the entire ray paths (0.5–0.8% in WSK02 and 2–2.5 % in WSK04).

4.2. Poststimulation Seismicity

Our data show minimal variations in focal mechanism before and after the mainshock, indicating that changes in apparent fast splitting direction or/and splitting time are predominantly due to changes in seismic anisotropy in the subsurface. As shown in Figure 3, the splitting measurements from clusters POST1 and POST2 indicate a 60–70% reduction in seismic anisotropy after the mainshock, whereas the low δt (less than 0.02 s) is comparable to the measurements from HF1.

We suggest that, at the moment of rupture, a surrounding fault damage zone (Kim et al., 2004) is expected to be around the main slip zone with numerous juxtaposed fractures or small-scale faults in the cataclastic shale formation (Billi et al., 2003; Huang, 2018). The width of the damage zone is influenced by fault strength, lithology, diagenesis, and fluids (Childs et al., 2009), and such a damage zone could potentially disrupt the hydraulic fractures in the immediate surrounding the HF well. Furthermore, the ruptured faults may serve as conduits by which hydraulic fluid escapes, resulting in the closure of fluid-filled fractures (Gudmundsson et al., 2001). Fluid flow-back may have also contributed to the reduced anisotropy. However, since the HF operations ceased immediately after the last stage of stimulation, the bulk of the injected fluid was retained underground after the stimulations and the effect of flow-back on the post-event fluid loss may be secondary. In addition, strain changes caused by relatively large seismic events may alter the velocities of the *S* waves in different strain directions. The increased *S* wave velocity parallel to the N-S compressive stress orientation (Zuo et al., 2018) can further contribute to the temporal variations in seismic anisotropy. Overall, we conclude that the minimal splitting time measured from the poststimulation seismicity may reflect the increased complexity (i.e., fluid loss) of faults and hydraulic fractures surrounding the HF well. Therefore, the mainshock effectively recalibrated the seismic anisotropy and returned the subsurface to the less disturbed state (N-S trending fault anisotropy) at the early stage of HF. This is evidenced by the similar δt and Φ observed from POST1 and HF1 (Figure 3d) and further reduced anisotropy observed at a much later stage from POST2.

In summary, the apparent spatiotemporal variation of anisotropy leads to a 3-D conceptual model where the faults and hydraulic fractures are present in the vicinity of the horizontal HF well (Figure 4b). We can separate the apparent anisotropy into two components: (1) stationary component caused by the N-S trending faults and (2) a time-dependent component caused by the NE-SW fluid-filled fractures and was reduced after the mainshock. Further insights could be gained from the spatiotemporal variations in these two components (Figure 4c). It has been reported that the amount of anisotropy caused by HF in the Duvernay shale can reach up to 30% in rock physical experiments (Ong et al., 2016). The thickness of the total shale formation is over 90 m (Davis & Karlen, 2014) and, due to the nearly parallel emergence angle, the range of anisotropy within the HF area is estimated to be 200–400 m, which accounts for 5–10% of the lengths of ray paths. Although the depth and location of anisotropic layers are nonunique since δt represents anisotropy over the entire ray paths, a back-of-the-envelope calculation (see Text S3) would suggest that fluid-filled fractures likely contribute to an average of 1.5–2% anisotropy, which represents about 70–80% of the apparent anisotropy (i.e., 2–2.5%). The remaining parts are attributed to the faults/folds. Although the observed splitting parameters are not simply a vector summation of the two contributing factors (Silver & Savage, 1994), the apparent anisotropy likely falls within the acute angle between the NE-SW fractures and near N-S faults, as evidenced by the results at stations WSK02 and WSK04. After the mainshock, most hydraulic fractures are closed (Figure 4c) due to the loss of fluids to the fault damage zone, and fracture-induced anisotropy is greatly reduced (i.e., a shorter fracture vector in Figure S22), while the fault contribution remains largely unchanged after the mainshock. Overall, the magnitude of the apparent anisotropy is reduced, and the fast splitting direction exhibits a counterclockwise rotation by ~25° toward the N-S direction in WSK04.

It is conceivable that the damage zone may represent a "fracture mesh system" that complicates the anisotropic structure near the shale gas development site (Figure 4b). This system could provide greater connectivity and additional channels for shale gas migration (Fisher et al., 2005; Jahandideh & Jafarpour, 2016). A future study of time-lapse analysis may offer further insights into the spatiotemporal variations in regional anisotropy and the focal mechanisms associated with induced earthquakes.

5. Conclusions

This paper presents the focal mechanisms and local seismic anisotropy using near-source recordings of the January 2016 induced earthquake swarm near Fox Creek, Alberta. The predicted *S* wave polarization from synthetic tests and splitting-corrected *S* wave polarization verify the robustness of all the measurements. The induced earthquakes during HF can be separated into two types of focal mechanisms: (1) those to the west of the mainshock (HF1, HF2, and POST1) that share a predominantly N-S strike-slip mechanism with high dip angles and (2) the eastern counterpart (POST2) that are more NE-SW striking while exhibiting slightly lower dip angles. Together, these mechanisms are consistent with the reported flower fault structures around the HF well and indicate no apparent temporal variations before and after the mainshock. The NE-SW fast splitting direction is a result of the superposition of faults and hydraulic fractures anisotropy. The 60–70% reduction in the strength of anisotropy is observed after the mainshock, suggesting that the fault ruptured during the mainshock may have disrupted/closed the NE-SW-aligned fluid-filled fractures. Loss of fluid from hydraulic fractures into the fault damage zone can be viewed as a means to return the seismic anisotropy to a less disturbed state at the early stage of HF. Seismic anisotropy lends new insights on how HF impacts the surrounding subsurface structure. Its sensitivities to the stress field and fluids enable a timely evaluation of the state and development of faults and fractures networks, which will be critical for monitoring and mitigating induced earthquakes.

Acknowledgments
The injection data and seismographs were shared by the industry through Alberta Geological Survey at the Alberta Energy Regulator. Three-component waveforms and earthquake catalog from 4 to 19 January 2016 could be accessed through the website (https://sites.google.com/a/ualberta.ca/induced-earthquakes/). The authors are grateful to Gavin Hayes, Ryan Schultz, and Thomas Goebel for their insightful reviews. This work was jointly funded by the Future Energy Systems at the University of Alberta, the National Natural Science Foundation of China (grant 51704309), and the Fundamental Research Funds for the Central Universities (18CX07008A). T.-R. A. Song acknowledges the support by the Natural Environment Research Council, UK (NE/P001378/1).

References

Anderson, D. L., Minster, B., & Cole, D. (1974). The effect of oriented cracks on seismic velocities. *Journal of Geophysical Research*, *79*(26), 4011–4015. https://doi.org/10.1029/JB079i026p04011

Ando, M., Ishikawa, Y., & Yamazaki, F. (1983). Shear wave polarization anisotropy in the upper mantle beneath Honshu, Japan. *Journal of Geophysical Research*, *88*(B7), 5850–5864. https://doi.org/10.1029/JB088iB07p05850

Atkinson, G. M., Eaton, D. W., Ghofrani, H., Walker, D., Cheadle, B., Schultz, R., et al. (2016). Hydraulic fracturing and seismicity in the Western Canada Sedimentary Basin. *Seismological Research Letters*, *87*(3), 631–647. https://doi.org/10.1785/0220150263

Balfour, N. J., Cassidy, J. F., & Dosso, S. E. (2012). Crustal anisotropy in the forearc of the Northern Cascadia Subduction Zone, British Columbia. *Geophysical Journal International*, *188*(1), 165–176. https://doi.org/10.1111/j.1365-246X.2011.05231.x

Ballard, D. H. (1981). Generalizing the Hough transform to detect arbitrary shapes. *Pattern Recognition*, *13*(2), 111–122. https://doi.org/10.1016/0031-3203(81)90009-1

Bao, X., & Eaton, D. W. (2016). Fault activation by hydraulic fracturing in western Canada. *Science*, *354*(6318), 1406–1409. https://doi.org/10.1126/science.aag2583

Barth, A., Reinecker, J., Kurfeß, D., & Müller, B. (2010). Global crustal stress pattern based on the World Stress Map database release 2008. *Tectonophysics*, *482*(1–4), 3–15. https://doi.org/10.1016/J.TECTO.2009.07.023

Ben-Menahem, A., Gibson, R. L., & Sena, A. G. (2007). Green's tensor and radiation patterns of point sources in general anisotropic inhomogeneous elastic media. *Geophysical Journal International*, *107*(2), 297–308. https://doi.org/10.1111/j.1365-246X.1991.tb00827.x

Billi, A., Salvini, F., & Storti, F. (2003). The damage zone-fault core transition in carbonate rocks: Implications for fault growth, structure and permeability. *Journal of Structural Geology*, *25*(11), 1779–1794. https://doi.org/10.1016/S0191-8141(03)00037-3

Booth, D. C., & Crampin, S. (1985). Shear-wave polarizations on a curved wavefront at an isotropic free surface. *Geophysical Journal International*, *83*(1), 31–45. https://doi.org/10.1111/j.1365-246X.1985.tb05154.x

Bowman, J. R., & Ando, M. (1987). Shear-wave splitting in the upper-mantle wedge above the Tonga subduction zone. *Geophysical Journal International*, *88*(1), 25–41. https://doi.org/10.1111/j.1365-246X.1987.tb01367.x

Childs, C., Manzocchi, T., Walsh, J. J., Bonson, C. G., Nicol, A., & Schöpfer, M. P. J. (2009). A geometric model of fault zone and fault rock thickness variations. *Journal of Structural Geology*, *31*(2), 117–127. https://doi.org/10.1016/J.JSG.2008.08.009

Chopra, S., Sharma, R. K., Ray, A. K., Nemati, H., Morin, R., Schulte, B., & D'Amico, D. (2017). Seismic reservoir characterization of Duvernay shale with quantitative interpretation and induced seismicity considerations—A case study. *Interpretation*, *5*(2), T185–T197. https://doi.org/10.1190/INT-2016-0130.1

Courtier, A. M., Gaherty, J. B., Revenaugh, J., Bostock, M. G., & Garnero, E. J. (2010). Seismic anisotropy associated with continental lithosphere accretion beneath the CANOE array, northwestern Canada. *Geology*, *38*(10), 887–890. https://doi.org/10.1130/G31120.1

Crampin, S. (1987). Geological and industrial implications of extensive-dilatancy anisotropy. *Nature*, *328*(6130), 491–496. https://doi.org/10.1038/328491a0

Crampin, S. (1991). Wave propagation through fluid-filled inclusions of various shapes: Interpretation of extensive-dilatancy anisotropy. *Geophysical Journal International*, *104*(3), 611–623. https://doi.org/10.1111/j.1365-246X.1991.tb05705.x

Davis, M., & Karlen, G. (2014). A regional assessment of the Duvernay Formation; a world-class liquids-rich shale play. Calgary, Canada: GeoConvention: Integration. Retrieved from http://www.searchanddiscovery.com/documents/2014/10638davis/ndx_davis.pdf

Eaton, D. W., Igonin, N., Poulin, A., Weir, R., Zhang, H., Pellegrino, S., & Rodriguez, G. (2018). Induced seismicity characterization during hydraulic-fracture monitoring with a shallow-wellbore geophone array and broadband sensors. *Seismological Research Letters*, *89*(5), 1641–1651. https://doi.org/10.1785/0220180055

Eken, T., Bohnhoff, M., Bulut, F., Can, B., & Aktar, M. (2013). Crustal anisotropy in the Eastern Sea of Marmara Region in Northwestern Turkey. *Bulletin of the Seismological Society of America*, *103*(2A), 911–924. https://doi.org/10.1785/0120120156

Ellsworth, W. L. (2013). Injection-induced earthquakes. *Science*, *341*(6142), 1225942. https://doi.org/10.1126/science.1225942

Faccenda, M., Burlini, L., Gerya, T. V., & Mainprice, D. (2008). Fault-induced seismic anisotropy by hydration in subducting oceanic plates. *Nature*, *455*(7216), 1097–1100. https://doi.org/10.1038/nature07376

Fischer, T., Hainzl, S., Eisner, L., Shapiro, S. A., & Le Calvez, J. (2008). Microseismic signatures of hydraulic fracture growth in sediment formations: Observations and modeling. *Journal of Geophysical Research*, *113*, B02307. https://doi.org/10.1029/2007JB005070

Fisher, M. K., Wright, C. A., Davidson, B. M., Steinsberger, N. P., Buckler, W. S., Goodwin, A., & Fielder, E. O. (2005). Integrating fracture mapping technologies to improve stimulations in the Barnett Shale. *SPE Production & Facilities*, *20*(02), 85–93. https://doi.org/10.2118/77441-PA

Galloway, E., Hauck, T., Corlett, H., Pană, D., & Schultz, R. (2018). Faults and associated karst collapse suggest conduits for fluid flow that influence hydraulic fracturing-induced seismicity. *Proceedings of the National Academy of Sciences of the United States of America*, *115*(43), E10003–E10012. https://doi.org/10.1073/pnas.1807549115

Gavin, L. J., & Lumley, D. (2016). Stress-induced seismic azimuthal anisotropy in the upper crust across the North West Shelf, Australia. *Journal of Geophysical Research: Solid Earth*, *121*, 1023–1039. https://doi.org/10.1002/2015JB012568

Grigoli, F., Cesca, S., Rinaldi, A. P., Manconi, A., López-Comino, J. A., Clinton, J. F., et al. (2018). The November 2017 Mw 5.5 Pohang earthquake: A possible case of induced seismicity in South Korea. *Science*, *360*(6392), 1003–1006. https://doi.org/10.1126/science.aat2010

Gudmundsson, A., Berg, S. S., Lyslo, K. B., & Skurtveit, E. (2001). Fracture networks and fluid transport in active fault zones. *Journal of Structural Geology*, *23*(2–3), 343–353. https://doi.org/10.1016/S0191-8141(00)00100-0

Huang, Y. (2018). Earthquake rupture in fault zones with along-strike material heterogeneity. *Journal of Geophysical Research: Solid Earth*, *123*, 9884–9898. https://doi.org/10.1029/2018JB016354

Huang, Z., Zhao, D., & Wang, L. (2011). Shear wave anisotropy in the crust, mantle wedge, and subducting Pacific slab under northeast Japan. *Geochemistry, Geophysics, Geosystems*, *12*, Q01002. https://doi.org/10.1029/2010GC003343

Jahandideh, A., & Jafarpour, B. (2016). Optimization of hydraulic fracturing design under spatially variable shale fracability. *Journal of Petroleum Science and Engineering*, *138*, 174–188. https://doi.org/10.1016/J.PETROL.2015.11.032

Kaneshima, S. (1990). Origin of crustal anisotropy: Shear wave splitting studies in Japan. *Journal of Geophysical Research*, *95*(B7), 11121. https://doi.org/10.1029/JB095iB07p11121

Kaneshima, S., Ando, M., & Kimura, S. (1988). Evidence from shear-wave splitting for the restriction of seismic anisotropy to the upper crust. *Nature*, *335*(6191), 627–629. https://doi.org/10.1038/335627a0

Kaviris, G., Spingos, I., Kapetanidis, V., Papadimitriou, P., Voulgaris, N., & Makropoulos, K. (2017). Upper crust seismic anisotropy study and temporal variations of shear-wave splitting parameters in the western Gulf of Corinth (Greece) during 2013. *Physics of the Earth and Planetary Interiors*, *269*, 148–164. https://doi.org/10.1016/J.PEPI.2017.06.006

Kim, Y.-S., Peacock, D. C., & Sanderson, D. J. (2004). Fault damage zones. *Journal of Structural Geology*, *26*(3), 503–517. https://doi.org/10.1016/J.JSG.2003.08.002

Langenbruch, C., & Zoback, M. D. (2016). How will induced seismicity in Oklahoma respond to decreased saltwater injection rates? *Science Advances*, *2*(11), e1601542. https://doi.org/10.1126/sciadv.1601542

Li, T., Wang, R., Wang, Z., & Wang, Y. (2016). Experimental study on the effects of fractures on elastic wave propagation in synthetic layered rocks. *Geophysics*, *81*(4), D441–D451. https://doi.org/10.1190/geo2015-0661.1

Li, Z., & Peng, Z. (2017). Stress- and structure-induced anisotropy in Southern California from two decades of shear wave splitting measurements. *Geophysical Research Letters*, *44*, 9607–9614. https://doi.org/10.1002/2017GL075163

Licciardi, A., Eken, T., Taymaz, T., Piana Agostinetti, N., & Yolsal-Çevikbilen, S. (2018). Seismic anisotropy in central North Anatolian Fault Zone and its implications on crustal deformation. *Physics of the Earth and Planetary Interiors*, *277*, 99–112. https://doi.org/10.1016/J.PEPI.2018.01.012

Long, M. D., & Silver, P. G. (2009). Shear wave splitting and mantle anisotropy: Measurements, interpretations, and new directions. *Surveys in Geophysics*, *30*(4–5), 407–461. https://doi.org/10.1007/s10712-009-9075-1

Maher, S., & Kendall, J.-M. (2018). Crustal anisotropy and state of stress at Uturuncu Volcano, Bolivia, from shear-wave splitting measurements and magnitude–frequency distributions in seismicity. *Earth and Planetary Science Letters*, *495*, 38–49. https://doi.org/10.1016/J.EPSL.2018.04.060

Meadows, M. A., & Winterstein, D. F. (1994). Seismic detection of a hydraulic fracture from shear-wave VSP data at Lost Hills Field, California. *Geophysics*, *59*(1), 11–26. https://doi.org/10.1190/1.1443523

Murray, R. S., & Schmitt, D. (2016). Fracking minimizing the risk (pp. 1–4). Calgary, Canada: Geoconvetion meeting.

Nagel, N. B., Sanchez-Nagel, M. A., Zhang, F., Garcia, X., & Lee, B. (2013). Coupled numerical evaluations of the geomechanical interactions between a hydraulic fracture stimulation and a natural fracture system in shale formations. *Rock Mechanics and Rock Engineering*, *46*(3), 581–609. https://doi.org/10.1007/s00603-013-0391-x

Nolte, K. A., Tsoflias, G. P., Bidgoli, T. S., & Watney, W. L. (2017). Shear-wave anisotropy reveals pore fluid pressure–induced seismicity in the U.S. midcontinent. *Science Advances*, *3*(12), e1700443. https://doi.org/10.1126/sciadv.1700443

Ong, O. N., Schmitt, D. R., Kofman, R. S., & Haug, K. (2016). Static and dynamic pressure sensitivity anisotropy of a calcareous shale. *Geophysical Prospecting*, *64*(4), 875–897. https://doi.org/10.1111/1365-2478.12403

Park, J., & Levin, V. (2002). Seismic anisotropy: Tracing plate dynamics in the mantle. *Science (New York, N.Y.)*, *296*(5567), 485–489. https://doi.org/10.1126/science.1067319

Peng, Z., & Ben-Zion, Y. (2005). Spatiotemporal variations of crustal anisotropy from similar events in aftershocks of the 1999 *M* 7.4 İzmit and *M* 7.1 Düzce, Turkey, earthquake sequences. *Geophysical Journal International*, *160*(3), 1027–1043. https://doi.org/10.1111/j.1365-246X.2005.02569.x

Rößler, D., Krüger, F., & Rümpker, G. (2007). Retrieval of moment tensors due to dislocation point sources in anisotropic media using standard techniques. *Geophysical Journal International*, *169*(1), 136–148. https://doi.org/10.1111/j.1365-246X.2006.03243.x

Saltzer, R. L., Gaherty, J. B., & Jordan, T. H. (2000). How are vertical shear wave splitting measurements affected by variations in the orientation of azimuthal anisotropy with depth? *Geophysical Journal International*, *141*(2), 374–390. https://doi.org/10.1046/j.1365-246x.2000.00088.x

Saruwatari, K., Ji, S., Long, C., & Salisbury, M. H. (2001). Seismic anisotropy of mantle xenoliths and constraints on upper mantle structure beneath the southern Canadian Cordillera. *Tectonophysics*, *339*(3–4), 403–426. https://doi.org/10.1016/S0040-1951(01)00136-6

Savage, M. K. (1999). Seismic anisotropy and mantle deformation: What have we learned from shear wave splitting? *Reviews of Geophysics*, *37*(1), 65–106. https://doi.org/10.1029/98RG02075

Schultz, R., Atkinson, G., Eaton, D. W., Gu, Y. J., & Kao, H. (2018). Hydraulic fracturing volume is associated with induced earthquake productivity in the Duvernay play. *Science (New York, N.Y.)*, *359*(6373), 304–308. https://doi.org/10.1126/science.aao0159

Schultz, R., Wang, R., Gu, Y. J., Haug, K., & Atkinson, G. (2017). A seismological overview of the induced earthquakes in the Duvernay play near Fox Creek, Alberta. *Journal of Geophysical Research: Solid Earth*, *122*, 492–505. https://doi.org/10.1002/2016JB013570

Shragge, J., Bostock, M. G., Bank, C. G., & Ellis, R. M. (2002). Integrated teleseismic studies of the southern Alberta upper mantle. *Canadian Journal of Earth Sciences*, *39*(3), 399–411. https://doi.org/10.1139/e01-084

Silver, P. G. (1996). Seismic anisotrophy beneath the continents: Probing the depths of geology. *Annual Review of Earth and Planetary Sciences*, *24*(1), 385–432. https://doi.org/10.1146/annurev.earth.24.1.385

Silver, P. G., & Chan, W. W. (1988). Implications for continental structure and evolution from seismic anisotropy. *Nature*, *335*(6185), 34–39. https://doi.org/10.1038/335034a0

Silver, P. G., & Chan, W. W. (1991). Shear wave splitting and subcontinental mantle deformation. *Journal of Geophysical Research*, *96*(B10), 16429. https://doi.org/10.1029/91JB00899

Silver, P. G., & Savage, M. K. (1994). The interpretation of shear-wave splitting parameters in the presence of two anisotropic layers. *Geophysical Journal International*, *119*(3), 949–963. https://doi.org/10.1111/j.1365-246X.1994.tb04027.x

Snoke, J. A. (1984). A program for focal mechanism determination by combined use of polarity and SV-P amplitude ratio data. *Earthquake Notes*, *55*(15), Retrieved from. https://ci.nii.ac.jp/naid/10009508266/

Song, T. A., & Kawakatsu, H. (2012). Subduction of oceanic asthenosphere: Evidence from sub-slab seismic anisotropy. *Geophysical Research Letters*, *39*, L17301. https://doi.org/10.1029/2012GL052639

Tarayoun, A., Audet, P., Mazzotti, S., & Ashoori, A. (2017). Architecture of the crust and uppermost mantle in the northern Canadian Cordillera from receiver functions. *Journal of Geophysical Research: Solid Earth*, *122*, 5268–5287. https://doi.org/10.1002/2017JB014284

Teanby, N. A., Kendall, J.-M., & van der Baan, M. (2004). Automation of Shear-Wave Splitting Measurements using Cluster Analysis. *Bulletin of the Seismological Society of America*, *94*(2), 453–463. https://doi.org/10.1785/0120030123

Wang, R., Gu, Y. J., Schultz, R., & Chen, Y. (2018). Faults and non-double-couple components for induced earthquakes. *Geophysical Research Letters*, *45*, 8966–8975. https://doi.org/10.1029/2018GL079027

Wang, R., Gu, Y. J., Schultz, R., Kim, A., & Atkinson, G. (2016). Source analysis of a potential hydraulic-fracturing-induced earthquake near Fox Creek, Alberta. *Geophysical Research Letters*, *43*, 564–573. https://doi.org/10.1002/2015GL066917

Wang, R., Gu, Y. J., Schultz, R., Zhang, M., & Kim, A. (2017). Source characteristics and geological implications of the January 2016 induced earthquake swarm near Crooked Lake, Alberta. *Geophysical Journal International*, *210*(2), 979–988. https://doi.org/10.1093/gji/ggx204

Wells, D. L., & Coppersmith, K. J. (1994). New empirical relationships among magnitude, rupture length, rupture width, rupture area, and surface displacement. *Bulletin of the Seismological Society of America*, *84*(4), 974–1002.

Wu, L., Gu, Y. J., Chen, Y., & Liang, H. (2019). Shear wave splitting discloses two episodes of collision-related convergence in western North America. *Journal of Geophysical Research: Solid Earth*, *124*, 2990–3010. https://doi.org/10.1029/2018JB016352

Zhang, H., Eaton, D. W., Rodriguez, G., & Jia, S. Q. (2019). Source-mechanism analysis and stress inversion for hydraulic-fracturing-induced event sequences near Fox Creek, Alberta. *Bulletin of the Seismological Society of America*, *109*(2), 636–651. https://doi.org/10.1785/0120180275

Zuo, Q., Tang, Y., Niu, F., Li, G., Chen, H., Tao, K., & Chen, B. (2018). Temporal variations of near-surface anisotropy induced by hydraulic fracturing at a shale play site in Southwest China. *Journal of Geophysical Research: Solid Earth*, *123*, 8032–8044. https://doi.org/10.1029/2018JB016037